M. V. Joisher, R. S. Bayliss III, M. K. Ranjram, R. S. Yang, A. Jurkov, and D. J. Perreault, “High-Performance High-Power Inductor Design for High-Frequency Applications,” presented at the 2024 IEEE Applied Power Electronics Conference and Exposition (APEC), Long Beach, CA, USA, 2024.

High-Performance High-Power Inductor Design for High-Frequency Applications

Mansi V. Joisher*, Roderick S. Bayliss III†, Mike K. Ranjram‡, Rachel S. Yang*, Alexander Jurkov§, and David J. Perreault*
*Massachusetts Institute of Technology, †University of California, Berkeley, ‡Arizona State University, §MKS Instruments, Inc.
Email : mjoisher@mit.edu

***Abstract*—Magnetic components significantly impact the performance and size of power electronic circuits. This is especially true at radio frequencies (rf) of many MHz and above. In the high-frequency (HF, 3-30 MHz) range, coreless (or “air-core”) inductors are conventionally used. These inductors have typical quality factors of 200-500 and are often the major contributor to a system’s overall loss and size. Even when they can achieve high-Q, air-core inductors can induce electromagnetic interference (EMI) and eddy current loss in surrounding components, thus limiting system miniaturization. With recent advances in high-frequency magnetic materials, there is interest in design of cored inductors to achieve improved combinations of size and loss. This work investigates an approach to achieving high-power, high-frequency, high-Q cored inductors. The proposed design approach leverages high-frequency magnetic materials, core geometry, quasi-distributed gaps, and a shield winding to realize high-frequency inductors that emit little flux outside their physical volume. Design guidelines for such inductors are introduced and experimentally verified with a 500 nH inductor (Q = 1150) designed to operate at 13.56 MHz with a peak ac current of up to 80 Amps.**

I. Introduction

High-power inductors operating in the high-frequency (HF, 3-30 MHz) range are needed for applications such as rf plasma generation, induction heating, and HF wireless power transfer (e.g., [1]–[3]). Moreover, HF magnetics are a key technology to enable miniaturized switched-mode power converters operating at HF [4]. However, the design of efficient power inductors for HF operation is challenging. Inductors at lower frequencies are often constructed with a core to enable miniaturization and high efficiency, and to limit external flux. However, as the operating frequencies increase into the HF range, both copper and core losses become significant obstacles to the design of cored magnetics.

Commonly-used core materials for power applications like MnZn ferrites tend to exhibit poor performance with high core losses above a few MHz [5]. Additionally, skin effect and proximity effect increase conductor ac resistance at HF and make it challenging to efficiently carry large currents at HF frequencies [6]. Techniques such as using litz wire to reduce these losses become increasingly difficult at frequencies beyond a few MHz due to manufacturing constraints [5]. Consequently, air-core (coreless) inductors are prevalent in rf applications, and dominate the HF (3-30 MHz) and VHF (30-300 MHz) frequency ranges (e.g., [7], [8]).

While air-core inductors are simple and easy to fabricate, they suffer from significant drawbacks. The absence of a core means that the magnetic field generated by the inductor is not shielded and can couple with other components in the system. This often results in electromagnetic interference (EMI) and significant losses due to eddy currents. As a result, rf air-core inductors often require a significant physical volume and may need to be placed in a metal enclosure, isolated from the control circuitry, to mitigate EMI and preserve high efficiency [8], [9]. Consequently, air-core rf inductors can be a major bottleneck for system miniaturization and overall efficiency.

The strong desire to achieve higher efficiencies and power densities for rf applications has led to tremendous progress in the development, measurement, and characterization of high-performance magnetic materials. It has been found that low-permeability NiZn ferrite materials are particularly suitable for high-frequency ac inductor design (e.g., [10], [11]). Proper design of cored inductors leveraging these materials can provide better combinations of size and efficiency than coreless inductors [12]–[16].

The performance of cored HF inductors can benefit greatly from design techniques that mitigate the adverse effects of skin and proximity losses. Techniques such as field balancing [13]–[15] to reduce skin effect loss and single-layer windings and quasi-distributed gaps [17] to minimize proximity effect losses have shown potential in mitigating these challenges for moderate power levels at up to 3 MHz [13], [14]. Recent work presented in [15] using these design techniques and low-permeability NiZn magnetic materials has achieved impressive efficiency for high-power HF inductors at 13.56 MHz.

However, many of the designs above result in significant magnetic fields surrounding the inductor, with attendant concerns of EMI and eddy current losses. These effects become even more pronounced at higher frequencies and cannot be ignored. For instance, the high-power cored inductor described in [15] achieves impressive efficiency, but it still generates substantial external fringing flux, much like its air-core solenoid counterpart. The unshielded nature of this inductor’s external field can result in unwanted coupling with surrounding components, leading to induced losses and EMI. Consequently, there is a clear need for cored HF inductors that can provide both high efficiency and effective self-shielding.

We propose a self-shielded inductor that builds upon the cored inductor design discussed in [15]. As the name suggests, the self-shielded inductor is designed to ensure a minimal magnetic field outside the inductor’s physical volume. This is accomplished while maintaining many of the efficiency and

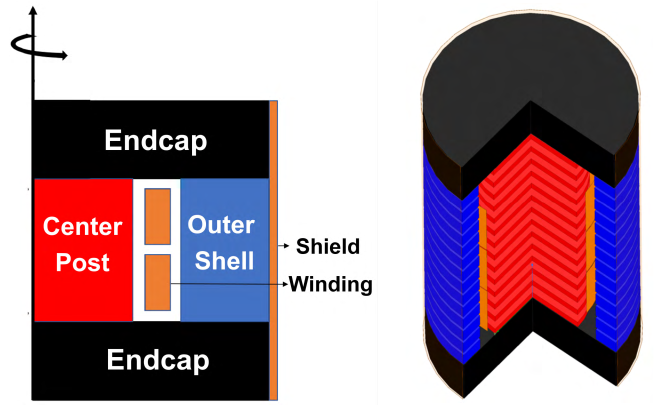

Fig. 1: Radial cross-section of the proposed inductor design, featuring the center post, outer shell, end caps, copper shield and a single-layer winding (left). 3D model with a transparent shield and a pie cut out for better visibility (right). The outer shell has notches that are not visible in these views.

performance benefits of the non-shielded HF inductor designs in [13]–[15].

Section II of the paper provides an overview of the proposed inductor structure. Section III offers guidelines for achieving low loss while effectively modeling and mitigating 3D effects that can become pronounced in designs having low turn counts. In Section IV, an example design is provided for a 500 nH inductor rated for a peak ac current of 80A at 13.56 MHz. Simulation results are provided that support the high-Q of the example design. In Section V, we detail the construction of a prototype based on the example design along with a measurement setup to experimentally verify both its performance and self-shielding characteristics. Section VI conducts a comparative evaluation between the proposed inductor and a conventional air-core inductor.

II. Geometry Overview

The proposed inductor design comprises a specialized pot-core structure with an outer shield as illustrated in Fig. 1. It includes a center post, an outer shell, two end caps, a single-layer winding, and a copper shield. The center post and outer shell are constructed using a stack of magnetic and non-magnetic material to create a quasi-distributed-gap structure. The center post consists of layers of alternating discs, while the outer shell comprises alternating layers of rings, each having one or more notches to facilitate the entry and exit of the winding to the window area. The outer shell serves as a return path for the flux within the physical volume of the inductor. The single-layer copper foil winding has evenly-spaced turns wound around the center post and enters and exits through one of the notches in the outer shell. The end caps enclose the winding and are used to shape the flux path, reducing the axial fringing of the flux. The entire structure is wrapped in a copper shield, which rejects flux leakage flowing out of the structure. A basic magnetic circuit for this structure is shown in Fig. 2.

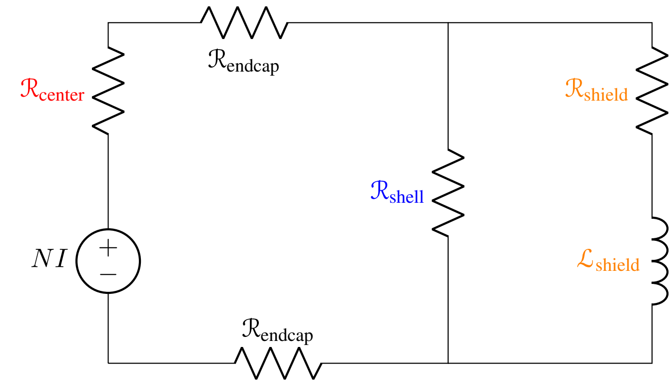

Fig. 2: Magnetic circuit model for the self-shielded inductor. The alternating core pieces and gaps in center post and outer shell are modeled as lumped reluctances. The lossy nature of the shield is modeled as a transferance element $\mathcal{L}_{\text{shield}}$ [18], [19].

III. Design Guidelines

To design and optimize the proposed inductor structure we use the model and design guidelines provided in this section. The optimal geometrical structure (Fig. 3) to maximize the quality factor (Q) is determined by minimizing total loss in the inductor for a given volume and inductance while adhering to some specific constraints discussed below.[1]

A. Quasi-distibuted Gaps and H-field Distribution

Leveraging design techniques from prior work in [13]–[15], the proposed design employs a pot core structure that carefully regulates the H-field distribution on both sides of the winding in a technique called field balancing. The improved H-field distribution allows a larger portion of the winding area to be utilized for current conduction than in typical designs, minimizing conduction loss associated with unused

[1]Inductor quality factor may be expressed as $Q = \frac{\omega L}{R_L}$, where L is the inductance, ω is the operating frequency, and R_L is the equivalent series resistance of the inductor [20]

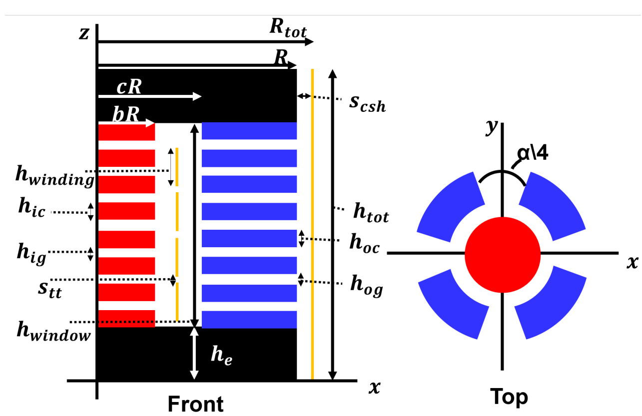

Fig. 3: Key parameters defining the geometry of the structure are labeled. A MATLAB optimization script systematically sweeps through these parameters to achieve a design that minimizes loss while adhering to the specified constraints.

conductor areas. Prior pot-core design approaches [13], [14] implement an even field balancing on either side of the winding to minimize conduction loss in the winding. Unlike in these designs, though, the proposed inductor design must also consider conduction losses in the outer shield when optimizing the field balancing in the core. With the introduction of the shield, the balance shifts towards a higher center post MMF percentage, approximately twice the outer shell MMF, to minimize conduction losses in the winding as well as the shield. Additionally, the proposed inductor design opts for a single-layer winding to minimize the proximity effect. Furthermore, by utilizing a single-layer copper foil for the winding, the proposed inductor can achieve a compact and space-efficient design.

An optimal cored magnetic design stores a large fraction of the total energy in the gaps of the structure [21]. In the realm of high-frequency and high-current applications, this tends to require large gaps. However, using large discrete gaps yields large fringing fields and consequent proximity effect losses. So, the gaps in the center post and outer shell structures are implemented using quasi-distributed gaps. The quasi-distributed gap structure allows for a more even distribution of the MMF across many small gaps. This prevents the fringing fields from being concentrated in a single gap and helps to mitigate fringing-field proximity-effect losses [17].

The reluctance of the center post ($\mathcal{R}_{\text{center}}$) in Fig. 2 is the sum of the total gap reluctance ($N_g \cdot \mathcal{R}_{\text{ig}}$) in series with the total center post core ($(N_g + 1) \cdot \mathcal{R}_{\text{ic}}$). Here, $\mathcal{R}_{\text{ig}}$ represents the reluctance of an individual center post gap piece, $\mathcal{R}_{\text{ic}}$ represents the reluctance of an individual center post core piece and N_g is the number of gaps. Similarly, the reluctance of the outer shell ($\mathcal{R}_{\text{shell}}$) can be expressed in terms of the reluctance of individual outer shell core and gap pieces ($\mathcal{R}_{\text{og}}$, $\mathcal{R}_{\text{oc}}$), and N_g.

The reluctances of the endcap, individual core, and gap pieces in the center post and outer shell can be directly calculated from the geometry (Fig. 3):

$$\mathcal{R}_{\text{ic}} = \frac{h_{ic}}{\mu_r \mu_0 \pi b^2 R^2} \qquad \mathcal{R}_{\text{ig}} = \frac{h_{ig}}{\mu_0 \pi b^2 R^2} \tag{1}$$

$$\mathcal{R}_{\text{oc}} = \frac{h_{oc}}{\mu_r \mu_0 \pi R^2 (1 - c^2)} \qquad \mathcal{R}_{\text{og}} = \frac{h_{og}}{\mu_0 \pi R^2 (1 - c^2)} \tag{2}$$

$$\mathcal{R}_{\text{endcap}} = \frac{(1 + c)}{\mu_r \mu_0 \pi 2 h_e} \tag{3}$$

B. Modeling and Mitigating Phi-directed Fields

To minimize total loss, core loss is traded against winding loss by selecting the number of turns [21]. In the HF design space, this often results in a low turn count. However, at low turn counts, the z-directed component of current owing to the helical nature of the winding creates a phi-directed component of the magnetic field in the outer core as shown in Fig. 4. If not addressed properly, this phi-directed field in the outer core can contribute significantly to the overall core loss in the system.

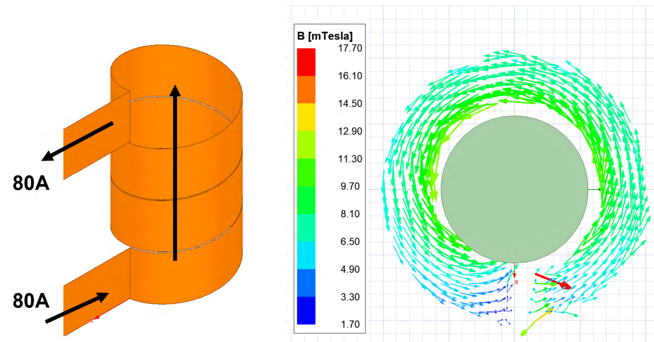

Fig. 4: Net z-directed current for an example design carrying 80A (left). Phi-directed field component in the outer shell due to the z-directed current, estimated to be 12mT, considerably larger than the z-directed field component, measuring 3.5mT (right)

Here we present one approach to minimize the loss component attributed to this phi-directed field.

The core loss in the outer core can be reduced by using one or more notches in the outer shell. In addition to providing a pathway for the winding to enter and exit the window, the notches serve to increase the reluctance of the phi-directed field path to reduce the phi-directed B-field. The notches, with a total notch angle α, are distributed symmetrically over the circumference, illustrated in the top view in Fig. 3, to mitigate fringing field issues that can arise from a single large notch.

The presence of phi-directed fields in the outer shell of the inductor not only contributes to core loss but also to the overall inductance of the structure. These fields, being orthogonal to the z-directed fields, store energy and affect the inductance characteristics. To model the contribution of these fields to the total loss and inductance, we developed the reluctance model for a single shell piece as shown in Fig. 5. The MMF generated by the z-directed current in the inductor winding creates a parallel path along each outer shell core piece and outer shell gap. The net phi-directed reluctance is expressed as the series combination of the outer shell core piece reluctance ($\mathcal{R}_{\text{osc}}$) and the notch reluctance ($\mathcal{R}_{\text{notch}}$), which is in parallel with the reluctance of the fringing field path around the notch ($\mathcal{R}_{\text{fringe}}$).

The shell, notch, and fringing field path reluctances are defined as :

$$\mathcal{R}_{\text{osc}} = \frac{(2\pi - \alpha)(1 + c)}{2\mu_0 \mu_r (1 - c) h_{\text{oc}}} \tag{4}$$

$$\mathcal{R}_{\text{notch}} = \frac{\alpha(1 + c)}{2\mu_0 (1 - c) h_{\text{oc}}} \tag{5}$$

$$\mathcal{R}_{\text{fringe}} = \frac{\alpha(1 + c)}{2\mu_0 (1 - c) h_{\text{og}}} \tag{6}$$

It should be noted that increasing the notch angle (α) also leads to a reduction in the available area for the z-directed field, resulting in a degradation of inductance. In this design space, we sweep the notch angle to strike a balance between minimizing total losses (i.e. maximizing Q), and considering the acceptable level of inductance degradation.

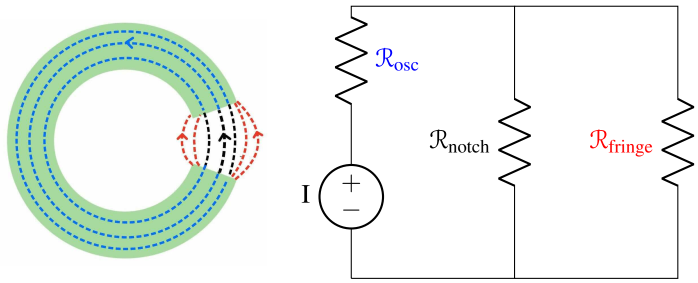

Fig. 5: Flux flow in an outer shell piece (left). Reluctance model for a single shell piece (right) consisting of the circumferential reluctance of a shell piece ($\mathcal{R}_{\text{osc}}$) in series with the parallel combination of the circumferential reluctance of shell notch ($\mathcal{R}_{\text{notch}}$) and the reluctance of the fringing path from the notch ($\mathcal{R}_{\text{fringe}}$). The outer shell notches are modeled as a lumped reluctance.

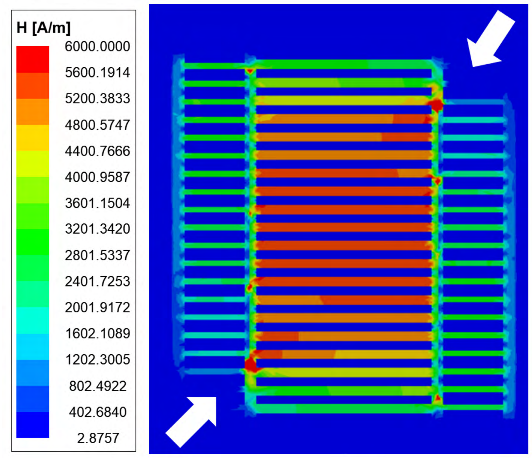

Fig. 6: H-field distribution on the YZ Cross-Section of an example 500 nH self-shielded Inductor, highlighting 'lost gaps' with arrows. The H-field gradually weakens in the gaps as we move from top to bottom on the left side and from bottom to top on the right side.

C. Modeling Lost Gaps

The helical nature of the winding introduces an asymmetry in how the circular core pieces are arranged compared to the evolution of the helical winding through the window. The turns of the winding are displaced in the z-direction by their height, and an additional spacing between turns. This displacement becomes particularly significant at the ends of the windings, altering the path of magnetic flux through this region. Fig. 6 highlights the tendency of fields to bridge the winding gap near the window ends. This reduces the overall reluctance of the core as some gaps are effectively bypassed, resulting in increased inductance, in addition to the added inductance from phi-directed fields.

To model the phenomenon of flux jumping across the winding window, we account for possible magnetic field paths. We assume the sole viable path is through sections of the window not blocked by the winding conductor. In our model, we incorporate reluctances associated with the "r-directed" window paths. This is based on the assumption that the winding resists flux passing through it. The effective reluctance for this window-jumping path is determined by:

$$\mathcal{R}_{\text{window}} = \frac{2}{\mu_0 \pi h_{\text{winding}}} \left(\frac{c-b}{c+b} \right) \tag{7}$$

We consider that this reluctance is connected in parallel with the number of outer core pieces and outer core gaps encompassed within the height of one winding turn. The number of lost gaps, $N_{\text{g,lost}}$, can be expressed as:

$$N_{\text{g,lost}} = \frac{h_{\text{winding}}}{h_{\text{og}} + h_{\text{oc}}} \tag{8}$$

Therefore, instead of considering the full reluctances of the outer core and outer gaps, we use a modified reluctance model illustrated in Fig. 7. By incorporating the concept of lost gaps, we are able to more accurately estimate the inductance for the design.

D. End Cap Flux Imbalance

A similar phenomenon is evident in the B-field distribution within the end caps, illustrated in Fig. 8. The B-field intensity remains low at the corners, indicating that the flux is traversing across the window. This observation implies an uneven distribution in the endcaps, with the entire volume not fully utilized. Nonetheless, since the endcaps lack gaps, their influence on the overall inductance is minimal. Therefore, we recommend manual adjustments to the endcap's height during simulation to further reduce the inductor's volume. A notable observation from Fig. 8 is the radial dependency of the B-field, which can be ascribed to the phi-directed field originating from z-directed currents.

E. Design Constraints

In addition to inductance and volume requirements, the optimized design must adhere to other specific constraints. These include the pitch-to-spacing ratio for quasi-distributed gaps [17], ensuring sufficient window area for the winding, and meeting feasible physical dimensions. Two critical constraints pertain to the self-resonant frequency (SRF) and the maximum magnetic flux density. The SRF is constrained to be four times

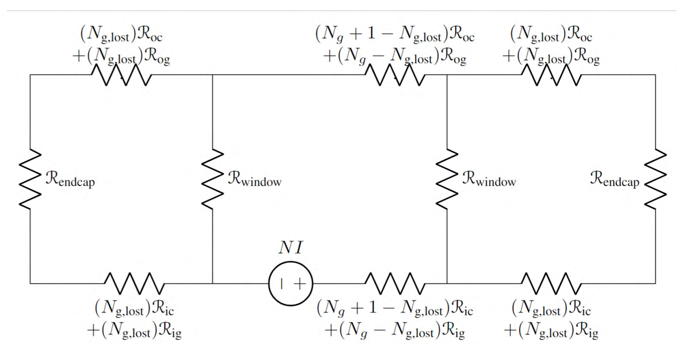

Fig. 7: Refined magnetic circuit model for z-directed fields accounting for the additional inductance due to lost gaps.

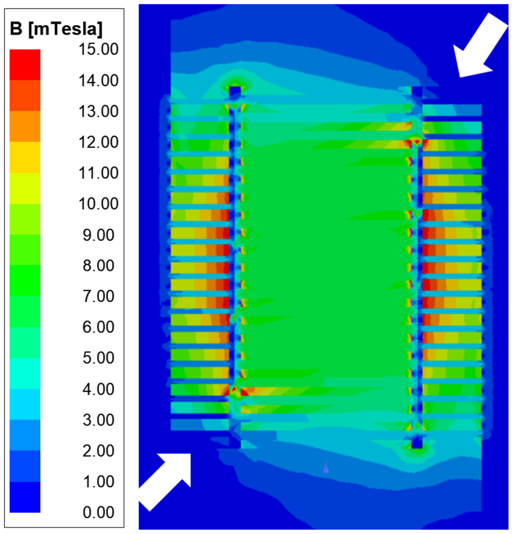

Fig. 8: B-field distribution on the YZ Cross-Section of an example 500 nH self-shielded inductor, highlighting the field imbalance in endcaps and radial dependency due to phi-directed fields.

the operating frequency, calculated using Knight's formula [22]. Additionally, the chosen Fair-rite 67 perminvar core material for the design example has a "whapping" threshold, a term used to describe the point at which the core material gets irreversibly damaged, of approximately 22 mT at 13.56 MHz [23], so maintaining the B-field below this limit is crucial to prevent irreversible changes in the material's properties and ensuring reliable inductor performance.

IV. Prototype Design and Simulation Results

As a test vehicle, a 500 nH inductor rated for $80A_{pk}$ at 13.56 MHz was designed following the design guidelines described above. Such an inductor is suitable for applications such as multi-kW matching networks (e.g., [8]). We developed a MATLAB script that employs a brute-force approach to search the parameter space and optimize the total loss for the given input parameters. The script optimizes the design by iteratively testing and refining different configurations, ensuring that the proposed design not only minimizes total loss but also meets the practical requirements of an inductor set by the specific constraints discussed above. Fair-rite's 67 core material ($\mu_r = 40$) is used due to its exceptional performance factor at the frequency of interest [11] [15].

The performance of this design was evaluated in ANSYS MAXWELL 3D and its thermal viability was assessed using ANSYS ICEPAK. As discussed in subsection III-D, the end caps are oversized and their height was fine-tuned in simulation to reduce the volume without impacting the inductance and total loss. The design specifications of the final self-shielded inductor are shown in Table I.

The simulated inductor achieved a Q of around 1495. For comparison, the proposed self-shielded inductor was compared

TABLE I: Design specification for the prototype self-shielded inductor

Volume	1.56 L
Inductance	500 nH
End-cap radius	51 mm
Center-post radius	27.7 mm
Outer-shell inner radius	38.64 mm
Winding radius	33.24 mm
Shield radius	51.92 mm
End-cap height	26.63 mm
Total height	192 mm
Number of gaps	13
Number of turns	3
Center-post core piece height	3.927 mm
Outer-shell core piece height	7.527 mm
Center-post spacer height	6.443 mm
Outer-shell spacer height	2.566 mm
Winding foil height	31.21 mm
Winding turn-to-turn spacing	1 mm
Winding foil thickness	50 μm
Total notch angle in outer shell	$\pi/3$
Number of notches	4
Core material	Fair-rite 67
Steinmetz parameters	$k = 1.779 \times 10^{-4}$ (mW/cm^3) $\alpha = 2.2$ (Hz), $\beta = 2.11$ (T)

to shielded air-core inductors[2] of equivalent inductance. The simulation results suggest that for the same total volume, the proposed inductor can achieve a 50% loss reduction compared to the shielded air-core inductor. While, for the same Q, the proposed self-shielded inductor can be realized in 0.28 times the volume of a shielded air-core inductor. The simulated loss distribution in the optimized design is shown in Fig. 9. The core loss to copper loss ratio slightly deviates from the optimum $2/\beta$ [21]. In this design context, this reflects a deliberate preference to place a higher emphasis on minimizing core loss over copper loss as ferrite is more susceptible to thermal stress.

V. Experimental Validation

A. Prototype Construction

The inductor was constructed using Fair-rite 67 NiZn core material. The center post and outer shell consist of 14 ferrite sections with 13 gaps, with the gaps defined by polypropylene spacers (Fig. 10). The winding is a 3-turn helix implemented using a 50 μm thick copper foil wound on a low-dielectric loss hollow Teflon cylinder (Fig. 10). A 3D-printed Ultem structure is used to hold together the outer core pieces and support the copper shield (Fig. 10). The small-signal inductance of the design was 570 nH and the SRF was found to be 50 MHz, close to our design target of 54 MHz, thus validating our model from Section III.

[2]Shielded air-core inductor: Air-core inductor placed inside a metal enclosure.

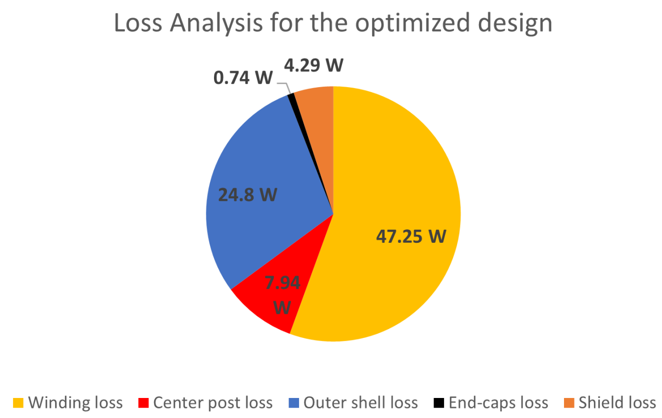

Fig. 9: Loss distribution in the optimized inductor, the total loss is 85 W. This analysis doesn't include dielectric loss.

B. Measurement Setup

It is challenging to experimentally determine the high-power Q of the inductor due to the non-linearity of the core loss, and the relatively small total loss in the inductor (equivalent series resistance of tens of milli-ohms). This low loss can be hard to differentiate from losses in the test setup [15]. The Q measurement setup shown in Fig. 11 and Fig. 12 is a modified version of the setup described in [15]. This setup features a series LC resonant tank, a transformer, and a tunable matching network, and is equipped with a voltage divider and optically isolated voltage probes for precise measurements. In this setup, the proposed self-shielded inductor is resonated with a low-loss vacuum capacitor and the input voltage and capacitor voltage are measured at resonance to determine the equivalent series resistance (R_L) of the inductor, using which Q can be determined. R_L is calculated using the following equations:

$$\frac{V_{\text{out,pk}}}{V_{\text{in,pk}}} = \left| \frac{1}{1 - \omega^2 CL + (j\omega C)(R_L + R_c + R_x)} \right| \tag{9}$$

At resonance:

$$\frac{V_{\text{out,pk}}}{V_{\text{in,pk}}} = \left| \frac{1}{j\omega C(R_L + R_c + R_x)} \right| \tag{10}$$

Fig. 10: Center post and one fourth of the outer shell stacked using core pieces and spacer material (left). Copper foil wrapped around center post through the PTFE support structure (center). Top view of the center post, outer shell and copper winding held together through the ultem support structure (right)

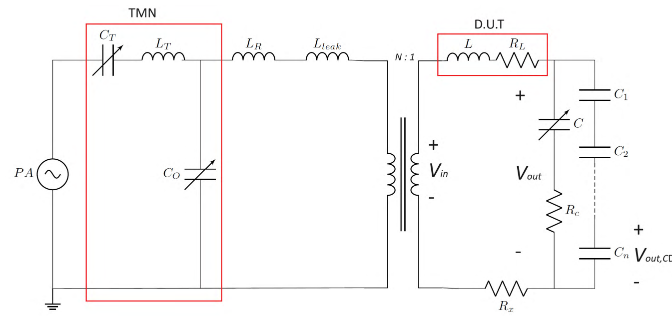

Fig. 11: Matching network and transformer coupled resonant tank experimental setup for Q-measurements at high frequency and high current level

$$R_L = \omega L \cdot \frac{V_{\text{in,pk}}}{V_{\text{out,pk}}} - R_x - R_c \tag{11}$$

Where R_c is the equivalent series resistance (ESR) of the vacuum capacitor and can be found in its datasheet. R_x is the additional resistance due to connecting leads of the inductor and can be estimated through FEA simulation.

The series resonant circuit is excited by a power amplifier (ENI A1000) through a transformer and a tunable matching network (TMN), MKS model MW2513. This combination serves to transform the low resonant impedance of the tank up to an acceptable load impedance for the power amplifier, and conversely step up the current from the power amplifier to drive the resonant tank. The current from the power amplifier is stepped up to excite the resonant tank in two stages: the TMN escalates it by a certain factor, after which the transformer further steps it up to reach higher drive levels (up to $80A_{pk}$) in the inductor. The TMN comprises a shunt variable vacuum capacitor and a series LC branch, which includes an air-core inductor and a variable vacuum capacitor. The capacitance of these variable capacitors can be adjusted, ensuring the impedance viewed by the power amplifier is always close to 50Ω. Additionally, the TMN serves as a low-pass filter, attenuating any higher-order harmonics that may be generated by the power amplifier under unfavorable conditions.

We begin the tuning process by adjusting the vacuum capacitor to ensure it resonates with the D.U.T at 13.56 MHz i.e. $|Z_{min}|$ @ 13.56 MHz. Next, we determine the impedance range for the TMN to output 50Ω. The number of primary turns on the transformer is adjusted such that $|Z_{min}|$ is within the TMN's resistive range, with the single secondary turn being the foil lead of the inductor. As the given TMN isn't intended to match for a purely resistive load, we introduce some reactance through a long coaxial cable (L_R). Lastly, we tune the variable capacitors in the TMN to get 50Ω at 13.56 MHz.

The transformer was implemented with 7 turns of triple-insulated litz wire (Rubadue wire, 230 strands/44 AWG litz, PN TXXL230/44F3XX-2(MW80)) on a Fair-rite 67 toroid (PN 5967003801). The leakage inductance (L_{leak}) of the

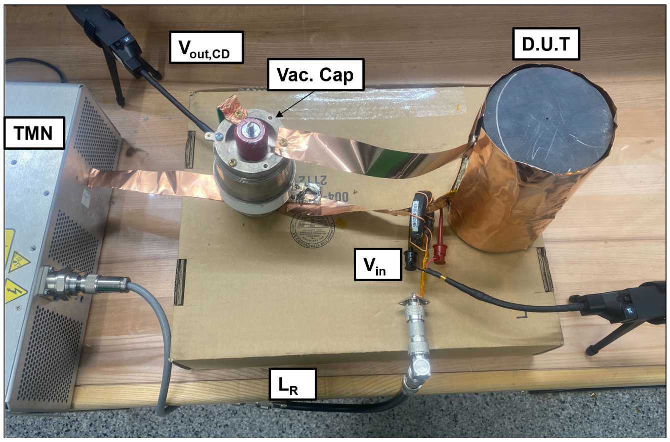

Fig. 12: An annotated photo of the test setup

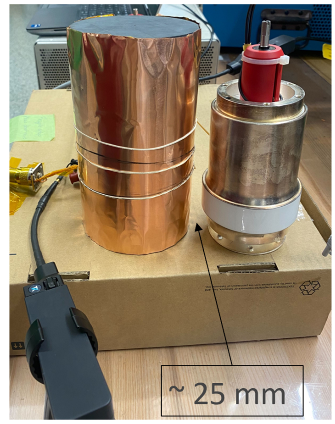

Fig. 13: Test setup to measure self-shielding characteristics of the proposed inductor in close proximity (25 mm) to a vacuum capacitor

transformer is calculated considering its series connection with the inductor under test. This combination resonates in conjunction with the vacuum capacitor.

Due to the high-quality resonance and substantial drive levels, a high voltage approximately 5kV at the full drive current of $80A_{pk}$, develops across the vacuum capacitor. Hence, a Comet-PCT 50-500 pF variable vacuum capacitor with a peak rf voltage capability of 9 kV (PN CVPO-500BC/15-BECA) and a low ESR (R_c = 4 mΩ at 13.56 MHz) was used to resonate with the D.U.T. A voltage divider using a series stack of ATC 100B capacitors was employed to measure this rf voltage.

One of the key challenges associated with such measurement setups as discussed in [15] is the presence of large common mode currents in the circuit. This issue is further exacerbated by the earth connection present on the oscilloscope, which provides a potential path for current flow. To minimize the common mode noise present in our measurement waveforms, we utilized optically isolated differential probes (Tektronix TIVP02), chosen specifically for their high Common Mode Rejection Ratio (CMRR) at our frequency of interest.

C. Q-Measurement Results

Experimental measurements confirm a Q of 1150 for a peak current of 80 amps, thereby demonstrating the high performance of the proposed approach. Multiple experiment iterations were performed to verify consistency and repeatability. The presence of common mode noise was assessed by connecting the test probes across the same potential. Common mode noise detected by the probes was less than 10% of the total signal, indicating minimal interference.

D. Self-Shielding Test

To validate the self-shielding feature of the proposed design, a vacuum capacitor with a significant metallic surface was placed close to the inductor in the measurement setup as shown in Fig. 13. The Q measurements were repeated in the presence of the vacuum capacitor and compared to the measurements from the previous case. The data demonstrates that the proximity of the vacuum capacitor to the inductor results in only a 8.7% reduction in quality factor at the maximum drive level, i.e., at $80A_{pk}$ current. The proposed inductor is still able to attain a high Q value of 1050, even with a large metallic object adjacent to it. These results affirm the self-shielding capabilities of the proposed design.

E. Simulated vs. Experimental Quality Factor

The difference between the simulated Q (1495) and the experimentally measured Q (1150) of the example inductor can be attributed to several factors. The use of copper foil, while reducing the required window space, can lead to issues during assembly, such as crumpling in the winding terminals, resulting in changes to resistance and loss that are challenging to simulate or quantify. The manual assembly of the inductor structure may result in non-concentric pieces, causing uneven field distribution and increased loss. The outer shell pieces surrounding the entry/exit notch for the winding terminal exhibit higher B-field at the edges in simulations, potentially inducing "whapping" (i.e. irreversible damage) in Fair-rite 67 material, which can alter the material's power loss curve. Modeling this phenomenon in simulations is difficult, and the extent of the piece's section affected by whapping remains unclear. The design also includes support structures, which use low-dielectric-loss plastics, and the simulation does not account for the dielectric loss component.

VI. Comparison with an Air-Core Inductor

A. Verification of the Measurement Setup

As a final step to affirm the credibility of the measurement setup, an air-core inductor was designed with an inductance nearly identical to our proposed inductor. This provides an opportunity to compare the quality factor measured at small signal amplitudes (using an impedance analyzer) to large signal measurements carried out with the matching network and transformer-coupled resonant tank setup.

The inductance of the air-core inductor measured using an impedance analyzer was found to be 585 nH. The air-core inductor was then resonated with a vacuum capacitor to a small-signal measurement for the loss in the inductor at resonance. The total impedance of this LC tank is a couple of mΩs. However, the impedance analyzer used (Agilent 4395A) is not capable of sensing such low values and hence, the 7:1 turn transformer was used to step up the impedance. The minimum impedance of the LC series tank at 13.56 MHz was found to be 60 mΩ indicating a small-signal Q of 820.

The large-signal measurement is done using the measurement guidelines discussed above. The large-signal Q was found to be approximately 750 for a peak current of $40A_{pk}$ at 13.56 MHz. The close alignment between the small-signal and large-signal Q measurements (factoring in the proximity losses linked with metal objects in proximity to the test bench) confirms the reliability and accuracy of the measurement setup.

B. Q-Degradation of the Air-Core Inductor

Next, a vacuum capacitor was placed next to the air-core inductor as done for the self-shielded inductor in Fig. 13 and the Q-measurements were repeated. It was observed that the Q of the air-core inductor dropped to 200 when placed in proximity to the vacuum capacitor. This underlines the severe adverse impact of placing metallic objects near air-core inductors, thereby underscoring a key benefit of self-shielded inductors.

VII. Conclusion

This paper presents a new self-shielded design for high-power inductors operating at radio frequencies (tens of MHz and hundreds of Watts and above). The design approach leverages previously used design techniques including the quasi-distributed gaps and field balancing. The design also addresses 3D effects that arise in such low-loss designs due to low turn count. A refined reluctance model is presented to enhance the optimization of the total loss in the inductor for a given inductance and volume. Simulation and experimental results show that the proposed design approach enables rf inductors of greatly improved combinations of size and efficiency as compared to the air-core inductors conventionally used in this frequency range. It is anticipated that the proposed passive component design will enable improved efficiency and miniaturization for high-power rf applications.

References

[1] A. S. Jurkov, A. Radomski, and D. J. Perreault, "Tunable matching networks based on phase-switched impedance modulation," *IEEE Transactions on Power Electronics*, vol. 35, no. 10, pp. 10 150–10 167, 2020.

[2] X. Zan, K. N. R. Islam, and D. J. Perreault, "Wide-range switched-mode power amplifier architecture," in *2023 IEEE 24th Workshop on Control and Modeling for Power Electronics (COMPEL)*, 2023, pp. 1–9.

[3] Haoquan Zhang, "Techniques for efficient wide-range radio-frequency power generation system," Doctoral dissertation, Massachusetts Institute of Technology, 2022.

[4] D. J. Perreault, J. Hu, J. M. Rivas, Y. Han, O. Leitermann, R. C. Pilawa-Podgurski, A. Sagneri, and C. R. Sullivan, "Opportunities and challenges in very high frequency power conversion," in *2009 Twenty-Fourth Annual IEEE Applied Power Electronics Conference and Exposition*, 2009, pp. 1–14.

[5] C. R. Sullivan, "Prospects for advances in power magnetics," in *CIPS 2016; 9th International Conference on Integrated Power Electronics Systems*, 2016, pp. 1–9.

[6] J. Kassakian, D. Perreault, G. Verghese, and M. Schlecht, *Principles of Power Electronics*, 2nd ed. Cambridge University Press, 2023, ch. 21.

[7] G. Zulauf and J. M. Rivas-Davila, "Single-turn air-core coils for high-frequency inductive wireless power transfer," *IEEE Transactions on Power Electronics*, vol. 35, no. 3, pp. 2917–2932, 2020.

[8] A. Al Bastami, A. Jurkov, D. Otten, D. T. Nguyen, A. Radomski, and D. J. Perreault, "A 1.5 kw radio-frequency tunable matching network based on phase-switched impedance modulation," *IEEE Open Journal of Power Electronics*, vol. 1, pp. 124–138, 2020.

[9] T. Simpson, "Effect of a conducting shield on the inductance of an air-core solenoid," *IEEE Transactions on Magnetics*, vol. 35, no. 1, pp. 508–515, 1999.

[10] Y. Han, G. Cheung, A. Li, C. R. Sullivan, and D. J. Perreault, "Evaluation of magnetic materials for very high frequency power applications," *IEEE Transactions on Power Electronics*, vol. 27, no. 1, pp. 425–435, 2012.

[11] A. J. Hanson, J. A. Belk, S. Lim, C. R. Sullivan, and D. J. Perreault, "Measurements and performance factor comparisons of magnetic materials at high frequency," *IEEE Transactions on Power Electronics*, vol. 31, no. 11, pp. 7909–7925, 2016.

[12] Y. Han and D. J. Perreault, "Inductor design methods with low-permeability rf core materials," *IEEE Transactions on Industry Applications*, vol. 48, no. 5, pp. 1616–1627, 2012.

[13] R. S. Yang, A. J. Hanson, B. A. Reese, C. R. Sullivan, and D. J. Perreault, "A low-loss inductor structure and design guidelines for high-frequency applications," *IEEE Transactions on Power Electronics*, vol. 34, no. 10, pp. 9993–10 005, 2019.

[14] R. S. Yang, A. J. Hanson, C. R. Sullivan, and D. J. Perreault, "Design flexibility of a modular low-loss high-frequency inductor structure," *IEEE Transactions on Power Electronics*, vol. 36, no. 11, pp. 13 013–13 024, 2021.

[15] R. S. Bayliss, R. S. Yang, A. J. Hanson, C. R. Sullivan, and D. J. Perreault, "Design, implementation, and evaluation of high-efficiency high-power radio-frequency inductors," in *2021 IEEE Applied Power Electronics Conference and Exposition (APEC)*, 2021, pp. 881–888.

[16] M. Solomentsev and A. J. Hanson, "At what frequencies should air-core magnetics be used?" *IEEE Transactions on Power Electronics*, vol. 38, no. 3, pp. 3546–3558, 2023.

[17] J. Hu and C. Sullivan, "The quasi-distributed gap technique for planar inductors: design guidelines," in *IAS '97. Conference Record of the 1997 IEEE Industry Applications Conference Thirty-Second IAS Annual Meeting*, vol. 2, 1997, pp. 1147–1152 vol.2.

[18] E. R. Laithewaite, "Magnetic equivalent circuits for electrical machines," *Proceedings of the Institution of Electrical Engineers*, vol. 114, no. 11, pp. 1805–1809, November 1967.

[19] J. Kassakian, D. Perreault, G. Verghese, and M. Schlecht, *Principles of Power Electronics*, 2nd ed. Cambridge University Press, 2023, ch. 19.

[20] ——, *Principles of Power Electronics*, 2nd ed. Cambridge University Press, 2023, ch. 10.

[21] ——, *Principles of Power Electronics*, 2nd ed. Cambridge University Press, 2023, ch. 20.

[22] D. W. Knight. The self-resonance and self-capacitance of solenoid coils: applicable theory, models and calculation methods. [Online]. Available: https://www.g3ynh.info/zdocs/magnetics/appendix/self_res/self-res.pdf

[23] Fairrite, "Low loss 67 material for high frequency power applications," https://www.fair-rite.com/wp-content/uploads/2016/04/Low-Loss-67-Material-for-High-Frequency-Power-Applications-for-website.pdf.